**The following article appeared in International Journal of Chemical Reactor Engineering*, 16(11): 20170141, (2018)*. And may be found at: https://doi.org/10.1515/ijcre-2017-0141**

**R. Romero Toledo[1] / M. Bravo Sánchez[2] / G. Rangel Porras[3] / R. Fuentes Ramírez[1] / A. Pérez Larios[4] / A. Medina Ramirez[1] / M. Martínez Rosales[1]**

# Effect of Mg as Impurity on the Structure of Mesoporous $\gamma$-$Al_2O_3$: Efficiency as Catalytic Support in HDS of DBT

[1] Departamento de Ingeniería Química, Universidad de Guanajuato, Noria Alta S/n, Col. Noria Alta, Guanajuato, Gto., C.P. 36050, México, E-mail: r.romerotoledo@ugto.mx, Rosalba@ugto.mx, adriana.medina@ugto.mx, mercedj@ugto.mx
[2] Instituto Potosino de Investigación Científica y Tecnológica. División de Materiales avanzados, C.P. 78216, San Luis Potosí, México, E-mail: mariela.bravo@ipicyt.edu.mx
[3] Departamento de Química, Universidad de Guanajuato, Noria Alta S/n, Col. Noria Alta, Guanajuato, Gto., C.P. 36050, México, E-mail: gporras@ugto.mx
[4] Universidad de Guadalajara, Centro Universitario de los Altos, Carretera a Yahualica, KM. 7.5, Tepatitlán de Morelos, Jalisco, C.P. 47600, México, E-mail: alarios@cualtos.udg.mx

**Abstract:**
This work shows the study of two alumina materials synthesized from aluminum sulfate with different purity by hydrolysis-precipitation route. The main difference between the aluminum salt precursors was the lower cost of one of them which was due to the higher percentage of magnesium species as impurity. Both materials showed different mesoporous structure nano-fibrillar. The physic-chemical properties of these materials were studied by several characterization techniques as XRD, XRF, BET, $^{27}$Al MAS NMR, Pyridine adsorption FT-IR, FE-SEM/EDX, TEM and XPS. Furthermore, these materials were used as supports in the formulations of NiMo-based catalysts which were obtained by impregnation by the incipient wetness method of Ni and Mo salts in 3.3 and 15 wt. % respectively. The two NiMo/$\gamma$-$Al_2O_3$ sulfide catalysts were evaluated as catalysts in the reaction of hydrodesulphurization (HDS) of dibenzothiophene (DBT), using a high-pressure batch reactor at 350 °C and 3.1 MPa and time reaction of 5 $h^{-1}$. The NiMo/$\gamma$-$Al_2O_3$ catalyst prepared by aluminum sulfate of low purity and lower cost exhibited the highest HDS efficiencies, 95 %, respectively, which were mainly ascribed to the presence of Mg (0.9 wt. %) as impurity.

**Keywords:** $\gamma$-$Al_2O_3$, catalysts, nano-fibrillar, hydrodesulphurization, Low cost, dibenzothiophene

**DOI:** 10.1515/ijcre-2017-0141

**Received:** July 15, 2017; **Revised:** May 19, 2018; **Accepted:** May 28, 2018

## 1 Introduction

Aluminum oxide ($Al_2O_3$), traditionally referred to as alumina, is a very important industrial material which has many applications such as adsorbents (Lesaint et al. 2008; Wang et al. 2014), abrasives, dehydrants, electronics and optics materials and mechanical engineering to biomedical materials, ceramics (Witharana et al. 2012), catalyst and catalyst support (Čejka 2003; Wang et al. 2001), this is a much explored fine material that still stands in limelight owing to its extensive applications. The special interest in the gamma variety of alumina is due to its excellent properties as high thermal stability (Liu and Yang 2010; Zhang, Zhang, and Chan 2004), high mechanical resistance, good catalytic activity (Hosseini and Khosravi Nikou 2012), porosity and large surface area and surface chemical properties that can be either acidic or basic depending on the transition alumina structure and the degree of hydration and hydroxylation of the surface, which is a major attraction from catalytic/adsorption point of view (Del Angel et al. 2005; 2007; 2012; 2014; Zhang et al. 2016).

In particular, the alumina plays an important role commercially in many chemical processes such as: the Claus reaction, cracking, hydrocracking and hydrodesulphurization of petroleum, either as catalyst and/or catalyst support (Jun-Cheng et al. 2006; Sifontes et al. 2014). Many authors have emphasized that $\gamma$-$Al_2O_3$ with high pore volume may improve the adsorption performance if used as an adsorbent and as loading capacity if applied as a catalytic support to minimize diffusion and transport influences. In the applications of transitional alumina as catalytic support, the unique acidity or acid-basicity is a crucial property, because it implies good

**R. Romero Toledo** is the corresponding author.

dispersion of the supported active species. However, this depends on the type of precursor and process of syntheses. Structurally, all transition of alumina are disordered crystalline phases. Pseudoboehmite, a poorly ordered form of boehmite with a small primary particle size, is often a preferred precursor to transition alumina, because it typically affords derivatives with relatively high surface areas and pore volumes (Liu and Yang 2010), in addition, of being a cost-effective material for the obtaining of $\gamma$-$Al_2O_3$ (Panias and Krestou 2007). Particularly, alumina ($\gamma$-$Al_2O_3$) is formed from well disordered pseudoboehmite at a temperature over 450 °C, depending on the particle size (Boumaza et al. 2009; Pecharroman et al. 1999; 2008).

In the past years, numerous methods, including chemical vapor deposition (Gao, Ito, and Goto 2015), precipitation (Farag, Al Zoubi, and Endres 2009), cation-anion double hydrolysis (Xu et al. 2017), hydrothermal (Dubey et al. 2017; Xu et al. 2016), sol–gel process (Farag, Al Zoubi, and Endres 2009; Sun et al. 2016), among others have been explored to prepare nano-crystalline $\gamma$-$Al_2O_3$ powders with diverse microstructures and dimensions. However, all these processes demand intensive reaction considerations such as high temperature, sophisticated techniques, high purity of gas, adjustable gas flow rate, expensive raw materials and so on. Hence, it is necessary to develop a simple and cost-impact avenue for synthesis of $\gamma$-$Al_2O_3$. Compared with the above synthesis methods, hydrolysis precipitation route is relatively popular since it is easier, low-cost, environmentally friendly, enormous scale production, low-temperature process and no catalyst is required, and from of this synthesis route can be obtained materials with properties suitable for catalytic supports and/or adsorbents. The only disadvantage is that the materials prepared in aqueous solution are usually poor in terms of shape and size control. Moreover, alumina by hydrolysis-precipitation route can be obtained from many precursors, among the most commonly used are: chlorides, nitrates, and sulfates. On the other hand, the majority of synthesized alumina reports are from high purity reagents, which increases the cost of the catalyst. However, there are sulfates of aluminum in the market with certain impurities, which makes them low cost reagents. However, the presence of impurities can influence in alumina productivity and quality and consequently affect the oxide morphology and/or physic-chemical properties. Interestingly, even a tiny amount of impurities in the $Al_2O_3$ structure can exert a strong effect on the alumina acidity, including defects structural. On the other hand, there may be impurities (both natural and artificially added) that present advantages, benefiting the desired reaction and/or process.

One of the most important processes that have received worldwide level attention for several decades, since they play a crucial role in the removal of impurities (sulfur, nitrogen, metals) from crude oil feedstock, is the Hydrodesulphurization that is an important hydrotreating process (HDT). Due to increasingly stringent environmental regulations, the catalytic properties of hydrotreating catalysts require improvement to increase the fuel quality (Rana et al. 2005; 2008). However, which this target can be reached by modifying the support properties of the catalysts or by increasing the severity of the reaction. Among them, the modification of the support particularly and catalyst properties is more suitable and less expensive. Common supports for hydrodesulphurization of petroleum are alumina-based. However, several authors have reported that the incorporation of MgO, $SiO_2$, $TiO_2$ and $ZrO_2$ with $Al_2O_3$ modifies the nature of active phase interactions on the support surface, making it useful as a support for HDT catalysts and remarkable improvements in HDS activity of catalysts can be achieved (Aberuagba et al. 2002; Breysse et al. 2003; 2014). Although there are many publications related with the application of the $\gamma$-alumina as catalyst supports for many reactions, where other metallic species are added with the purpose to enhance solid characteristics such as surface area, porosity, thermal stability, acidity, among other; there are not a lot of studies about the synthesis of $\gamma$-$Al_2O_3$ from low cost raw salts with emphasis in the possible role of the magnesium as impurity in the alumina characteristics and its performance as catalyst support.

In the present work, the effect of the impurities presence in the aluminum precursors on the physical chemical properties of the $\gamma$-$Al_2O_3$ and its performance as catalytic support is studied. Synthesized supports were impregnated with Ni and Mo salts by the incipient wetness method, the catalysts were evaluated for the dibenzothiophene hydrodesulfurization reaction and its catalytic activity results are discussed in terms of the presence of Mg as an impurity in the $\gamma$-alumina product and their effect in the catalyst. The catalyst with Mg presence resulted more active than the high purity catalyst. This paper contributes to a basic understanding of the purity of the salt of aluminum and how influences physicochemical characteristics of mesoporous materials. This fundamental knowledge could be exploited in the design of new materials, as an alternative approach to prepare HDS catalysts of low cost.

## 2 Experimental and procedure

### 2.1 Materials

In the present study, the starting materials to obtain hydrated alumina ($\gamma$-$Al_2O_3$) were $Al_2(SO_4)_3 \bullet 18H_2O$, with a purity of 95 % (by weight, wt.), technical grade (TG), Alfa-Omega, S.A., $Al_2(SO_4)_3 \bullet 18H_2O$, with a purity of 99.98 % (wt.), analytical reagent grade (AR), Sigma-Aldrich, as precursor salts, distilled water (Karal S.A. de C.V) and anhydrous $NH_3$ gas (Praxair, 99.98 % (wt.)), as precipitant.

### 2.2 Syntheses of pseudoboehmite

$Al_2(SO_4)_3 \bullet 18H_2O$ TG and/or AR were dissolved into deionized water. The $Al_2(SO_4)_3 \bullet 18\ H_2O$, TG was filtered for removal of insoluble impurities (Matrix of silice and iron). Precursors were prepared by dropping saturated solution of aluminum sulfate into a solution of water and ammonia gas, under rigorous magnetic stirring, at temperature of 50–70 °C. The precipitated solution was filtered; the precipitated of pseudoboehmite was rinsed with distilled water two times respectively and then dried at 110 °C for 12 h. The phase change of pseudoboehmite to $\gamma$-$Al_2O_3$ was performed by thermal treatment at 500 °C for 4 h. The chemical reactions (1) and (2) occurred during synthesis and obtaining of the gamma phase:

Aqueous solution step:

$$Al_2(SO_4)_3 + 6NH_3 + 6H_2O \rightarrow 2AlOOH + 3(NH_4)_2SO_4 + 2H_2O \quad (1)$$

Calcination step:

$$2AlOOH \rightarrow \gamma - Al_2O_3 + H_2O \quad (2)$$

The synthesized alumina was labeled according to the purity of the precursor salt, such as: $Al_2(SO_4)_3$-TG ($Al_2O_3$-A) and $Al_2(SO_4)_3$-AR ($Al_2O_3$-B).

### 2.3 Catalysts preparation

The catalysts NiMo/$\gamma$-$Al_2O_3$ was prepared by impregnating of 3 g of support by wet incipient impregnation with a solution containing nickel nitrate (Fluka 98.5 %) and ammonium heptamolybdate (Fluka 99.0 %) dissolved in water (pH = 7.0) in adequate concentrations to obtain a final content of 3.3 wt.% NiO and 15.0 wt.% $MoO_3$, respectively. This catalyst was dried at 120 °C/4 h and calcined at 450 °C/4 h. Reduced and activated under a flow of $H_2S/H_2$ (15 % v/v with a flow rate 60 ml $min^{-1}$) at 400 °C (5 °C/min) for 4 h. The formulated catalysts were labeled, such as: $Al_2O_3$-A (NiMo/$Al_2O_3$-A) and $Al_2O_3$-B (NiMo/$Al_2O_3$-B).

### 2.4 Catalytic activity measurement

In this work, the HDS of DBT was carried out in a Parr model 4560 high-pressure batch reactor. The reactor was loaded with 0.3 g of catalyst and the reaction mixture (5 vol. % of DBT in n-heptane). The reactor was pressurized to 3.1 MPa with hydrogen and heated up till 350 °C. The average reaction time was 5 h and liquid samples were taken every half hour and analyzed by chromatography on a Hewlett Packard 4890 instrument equipped with a FID detector and HP-Ultra 2 (30 m 0.32 mm i.d.) column. From data of DBT conversion as a function of time, the reaction-rate constant for each catalyst was calculated by assuming DBT conversion to be pseudo-zero order reaction (k) according to the equation:

$$X_{DBT} = \frac{1 - n_{DBT}}{\eta_{DBT}} = \frac{k}{\eta_{DBT,0}} t \quad (3)$$

Where $x_{DBT}$ is the conversion fraction of DBT, $\eta_{DBT}$ = moles of DBT, $\kappa$ = pseudo-zero order reaction-rate constant, t = time in seconds and ($\kappa/\eta_{DBT,0}$) is the slope.

The HDS of DBT yields two main products: biphenyl (BP) through the so-called direct desulfurization pathway (DDS) and cyclohexylbenzene (CHB) and tetrahydrodibenzothiophene (THDBT) through the hydrogenative pathway (HYD). Since these two pathways are parallel and competitive, the selectivity (HYD/DDS) was determined by:

$$\frac{\text{HYD}}{\text{DDS}} = \frac{[\text{CHB}] + [\text{THDBT}]}{[\text{BP}]} \tag{4}$$

## 3 Characterization

The textural properties of supports were determined by $N_2$ adsorption-desorption with a Micromeritics, ASAP 2010. The samples were degassed at 200 °C for 3 h, under vacuum. Nitrogen adsorption isotherms were measured at liquid $N_2$ temperature (77 K), and $N_2$ pressures ranging from $10^{-6}$ to 1.0 $P/P_0$. The specific surface areas were calculated by means of the Brunauer–Emmett–Teller (BET) method and the pore size distribution was obtained according to the Barret–Joyner–Halenda (BJH) method. The crystalline properties of the supports were characterized by X-ray diffraction (XRD) using a Siemens D-500 diffractometer equipped with a Cu Kα radiation anode and wavelength k = 1.54 Å, operated at 10–85º 2θ, current of 30 kV and 20 mA. The crystalline structure was obtained with the Jade 6.5 program. The nature of acid sites for the oxide support was determined by pyridine adsorbed Fourier transformed infrared (Pyridine FT-IR) spectroscopy on a FT-IR Nicolet 470 instrument with a resolution of 1 $cm^{-1}$. The support was dehydrated at 300 ºC for 1 h under vacuum, followed by adsorption of purified pyridine at room temperature. Then, the sample was evacuated at different temperatures and the pyridine-adsorbed IR spectra were recorded. Solid-state nuclear magnetic resonance (NMR) measurements were made with a Bruker Avance III HD 400 spectrometer in a nominal field of 9.4 T at the Larmor frequency of 104 MHz. The $^{27}Al$ spectra were observed using a magic angle spinning (MAS) probe. For this rotors of 4 mm were used and a rotation frequency of approximately 11 kHz using as reference a solid sample of $Al(NO_3)_3 \bullet 9H_2O$ ($^{27}Al$, d = 0.0 ppm). The morphology of materials was studied by Scanning electron microscopy using a JEOL JSM 7600-F Field-Emission with an energy dispersive X-ray spectroscopy (EDX) attachment. Samples were suspended in isopropanol by sonication and then deposited on carbon coated copper grids. The microstructures of oxide aluminum supports were studied by high-resolution transmission electron microscopy (HRTEM) using a Philips Tecnai F20 microscope operating at 200 kV. The elemental quantification of supports and aluminum precursors were determined by high resolution wavelength dispersive Kα X-ray fluorescence spectra (XRF) were recorded by a NEX-CG RIGAKU spectrometer of cartesian geometry, equipped with a Pd anode X-ray tube. A gas flow was used of He for maintain an inert atmosphere. The applied power of the tube was 25 to 50 kV. The surface structural properties analysis was achieved using X-ray photoelectron spectroscopy. The system used was a PHI 5000 VersaProbe II (Physical Electronics), where photoelectrons are excited with a monochromatic Al-Kα source of 1486.7 eV of photon energy operating with a power of 25 W over a 100 µm spot. The base and analysis pressures were about $3X10^{-9}$ and $8X10^{-9}$ torr, respectively. Since the samples are insulating, a dual beam charge neutralization system was used consisting of low-energy electron beam and ion beam. Before analysis all the samples were outgassed during 16 hours in pre-chamber under a vacuum of 4 X $10^{-6}$ Torr.

## 4 Results and discussion

### 4.1 X-ray fluorescence (XRF) analysis

The aluminum precursors and synthesized alumina were analyzed by XRF spectrometry for quantitative determination of the impurities present. From this ratio was determined that the element that predominates as impurity and makes the difference between both reagents is the magnesium, which is in concentration of around of 1.1 wt. %, for aluminum sulfate of low cost ($Al_2(SO_4)_3$-TG) and 0.9 wt. % in the synthesized alumina ($Al_2O_3$-A), attributing that 0.2 wt. % was eliminated during the washes in obtaining the pseudoboehmite. On the other hand, was determined 0.5 wt. % S, attributed to ammonium sulfate ($(NH_4)_2SO_4$) as residue generated during the synthesis process of the alumina. It was also observed, that the small amounts of Ca and Fe determined in the aluminum precursor were removed during the synthesis process. The XRF results are shows in Table 1.

**Table 1:** XRF results of the average chemical composition of the precursor salts of aluminum and synthesized alumina.

| Sample | Al | Si | S | Mg | Ca | Fe | O |
|---|---|---|---|---|---|---|---|
| | Concentration (wt. %)[a] | | | | | | |
| $Al_2(SO_4)_3$-A | 7.53 | 0.06 | 13.8 | 1.1 | 0.01 | 0.03 | 78.5 |
| $Al_2(SO_4)$3-B | 7.88 | 0.08 | 14.5 | 0.0 | 0.0 | 0.0 | 77.5 |
| | Concentration (wt. %)[b] | | | | | | |
| $Al_2O_3$-A | 45.0 | 0.03 | 0.5 | 0.9 | 0.00 | 0.00 | 54.0 |
| $Al_2O_3$-B | 44.9 | 0.02 | 0.09 | 0.0 | 0.00 | 0.00 | 54.9 |

*Percentage extraction values are based on triplicate analysis.
[a] Precursor salts
[b] Synthesized Alumina

## 4.2 Powder x-ray diffraction (XRD) analyses

Figure 1(a) and (b) illustrate the XRD patterns at wide angles of $Al_2O_3$-A and $Al_2O_3$-B matrix for determined their crystalline properties, respectively. The X-ray diffraction pattern was performed at 10 – 80 ° an angle 2θ. The results of the XRD patterns wide angles show seven weak diffraction peaks at 2θ = 19.2, 31.0, 36.6, 39.3, 46, 61.5, and 67 °, which can be indexed as the (111), (220), (311), (222), (400), (511), and (440) reflections of γ-alumina according to (JCPDS card 10–0425). The Figure 1(a), present a disorder in the structure that is reflected in the unusual broadening of some X-ray diffraction peaks in the region 2θ = 20–48 °, which is attributed to a strong faulting on the (111), (110), and (100) in the spinel-like structure of these material. This fault occurs as individual and/or interconnecting defects on different plane families (Sakashita, Araki, and Shimada 2001) and according to the literature, this non spinel model is more stable than alternative spinel type structures (Wolverton and Hass 2000). Therefore, the presence of Mg as impurity produced this disorder in the structure, as is reported by several authors (Pan et al. 2017a). This similar phenomenon was also observed when other heteroatoms are present into mesoporous materials (Pan et al. 2015b; Zhang et al. 2008). Noteworthily, compared with the XRD pattern of $Al_2O_3$-B, $Al_2O_3$-A demonstrated a relatively stronger intensity of the (220) and (311) in their XRD patterns, corresponding to a remarkably increased mesoscopic order. Moreover, with the small amount present of Mg, a distinct shift toward lower angle in the position of the (220) diffraction peak is observed, representing an increase in the lattice parameter (d220) values.

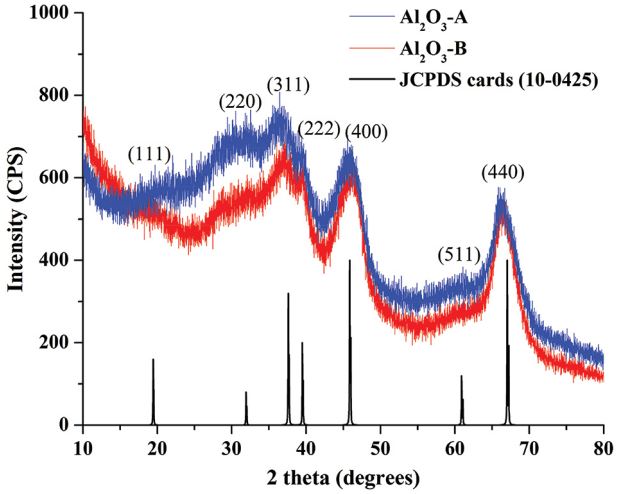


**Figure 1:** XRD patterns of $Al_2O_3$-A and $Al_2O_3$-B, JCPDS Cards: γ-$Al_2O_3$ (10–0425).

In concordance with Figure 1 and the Table 2, it is clearly evident that the evolution of the crystallite size is a function of the aluminum source and the synthesis. The crystallite size is different in both materials, presenting nanoparticle sizes. However, for $Al_2O_3$-A, this crystallite size is lower than in sample synthesized from aluminum sulfate of high purity. The crystallization of pseudoboehmite from aluminum sulfate of low purity is inhibited by the presence of sulfate anions present in the gel (Guzman-Castillo et al. 2005) of pseudoboehmite, observed in the $Al_2O_3$-A, as shown in the Table 1.

**Table 2:** Synthesis temperature and average crystal size of the γ-$Al_2O_3$ synthesized.

| Samples | Ts (ºC) | Crystal size[a] (Å) |
|---|---|---|
| | γ-AlOOH | γ-$Al_2O_3$ |
| $Al_2O_3$-A | 65 ± 3 | 16.3 |
| $Al_2O_3$-B | 65 ± 3 | 18.8 |

Ts: synthesis temperature
[a] From the software Jade 6.5

## 4.3 Morphology FE-SEM and TEM analyses

According to the results from XRD characterization, the samples resulted different in aluminum oxides with different crystallinity. FE-SEM and TEM images were of fundamental importance to understand the particle morphologies of the alumina samples by the proposed synthesis method in our study. Figure 2(a–b) shows the FE-SEM images of $Al_2O_3$-A and $Al_2O_3$-B samples.

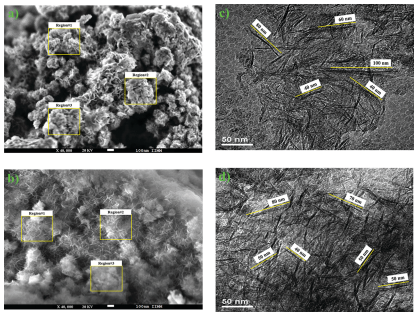

**Figure 2:** FE-SEM (a-b) with EDX analysis for three regions on the surface of the samples and TEM (c-d) images of samples, respectively. (a-c): $Al_2O_3$-A and (b-d): $Al_2O_3$-B.

FE-SEM/TEM images assigns nano-fibrillar size morphology for the agglomerates, both materials showed amorphous agglomerates due to their high surface energy, therefore; generating high porosity. Although both samples present pores type worm-hole channel/sponge, hinting to a highly interconnected porous system. Figure 2(c-d) shows the TEM images of the corresponding samples. The $Al_2O_3$-B sample presented a size of agglomerates more thinly, this due to the size of shorter fibers in average (80 nm lenght x 4 nm wide), as show in the TEM image. The $Al_2O_3$-A sample revealing that possesses a more porous structure, that $Al_2O_3$-B, presenting fibers size of around (100 nm long x 6 nm wide). These reduced dimensions may be related with the noticeable differences in the textural properties. In other words, the intercrossing degree and disorder among the fibers (inter-fibrillar porosity) as well as their length may cause the non-uniform pore size distributions which can extend up to 100 nm.

The composition of nano-particles in the samples was elucidated by Energy Dispersive Spectroscopy (EDX) conducted at 5 kV using spot mode. For our microanalyses a low kV (5 kV) was selected as it was deemed both suitable to generate X-rays for the major known elemental components of the sample (C, Al, Si, Ca, Mg, O, Fe, N and S), and would reduce sample charging that can compromise the results. The results show O, Al, S, N, Mg for $Al_2O_3$-A and O, Al, S for the $Al_2O_3$-B sample. These results are summarized in Table 3. The Al and O correspond to the stoichiometric composition of $Al_2O_3$. On the other hand, it was corroborated that the presence of Mg in the $Al_2O_3$-A sample, influenced the formation of Mg-O bonds with longer lengths than those of Al-O bonds, increasing the spacing and would result in a mesostructural expansion, as seen in Figure 1(a), due to this the difference in fiber sizes is attributed, being observed size fibers longer and wider in the $Al_2O_3$-A sample.

**Table 3:** Average elemental composition of $Al_2O_3$-A and $Al_2O_3$-B by Energy-dispersive X-ray (EDX).

| Samples | Concentration (wt. %) | | | | | | |
|---|---|---|---|---|---|---|---|
| | Al K | C K | S K | Mg K | N K | O K | Si K |

| | | | | | | | |
|---|---|---|---|---|---|---|---|
| $Al_2O_3$-A | 29.8 | 12.7 | 0.15 | 0.56 | 2.2 | 55.0 | 0.0 |
| $Al_2O_3$-B | 51.6 | 8.9 | 0.14 | 0.0 | 0.0 | 39.3 | 0.0 |

[1] Source: Author's own elaboration

## 4.4 $N_2$ physisorption

Figure 3 illustrates the $N_2$ adsorption–desorption isotherm and Barrett–Joyner–Halenda (BJH) pore size distribution curve. According to the classification made by IUPAC (Sing et al. 1985), the $N_2$ adsorption–desorption isotherm of both materials is found to be of type IV. Two well distinguished regions in the adsorption isotherm are evident: (i) monolayer–multilayer adsorption and (ii) capillary condensation. The first increase in adsorption at relative pressure P/P0 < 0.2 is due to multilayer adsorption on the surface, while the second increase at P/P0 = 0.44–0.97 for $Al_2O_3$-A and 0.49–0.97 for $Al_2O_3$-B, arises from capillary condensation in the mesoporous with nitrogen multilayers adsorbed on the inner surface. These materials show irregular shape isotherms with hysteresis loop type E indicate that the pores in the material have an inkwell-type shape. As can be seen from Figure 3(b, d), a relatively narrow pore size distribution (PSD) is detected, and the average BJH pore diameter calculated by using the adsorption branch data of the $N_2$ adsorption–desorption isotherms is about of 9.6 nm for $Al_2O_3$-A and 10.8 nm for the $Al_2O_3$-B.

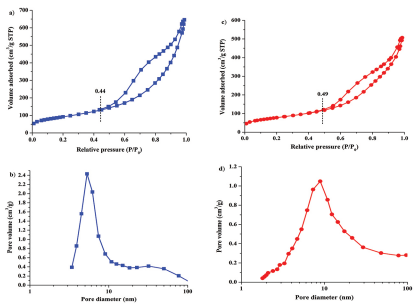

**Figure 3:** Adsorption-desorption isotherms of (a) $Al_2O_3$-A; (c) $Al_2O_3$-B; and the PSD of (b) $Al_2O_3$-A; and (d) $Al_2O_3$-B.

Table 4 shows the results of textural properties obtained in this work. The specific surface area (SSA), pore volume (PV) and average pore diameter (APD) is related to the particle size and crystallinity. However, the magnesium presence generated longer and wider fibers, leading to larger and slightly more crystalline agglomerates, in consequence the surface area of the material decreased for $Al_2O_3$-A compared with $Al_2O_3$-B, due this a small increase in specific surface area (about +42 $m^2/g$) is observed for the $Al_2O_3$-B, attributed to a smaller particle size, as is observed in the diffraction pattern, Figure 1(b) and TEM images, Figure 2(d).

**Table 4:** Textural properties obtained for $Al_2O_3$-A and $Al_2O_3$-B.

| Samples | SSA ($m^2 \bullet g^{-1}$) [a] | PV ($cm^3 \bullet g^{-1}$) [b] | APD (nm)[c] |
|---|---|---|---|
| $Al_2O_3$-A | 249 | 0.66 | 9.6 |
| $Al_2O_3$-B | 291 | 0.76 | 10.8 |

[a] Calculated with the BET-equation.
[b] Measured at $p/p_0 = 0.99$.
[c] Pore diameter determined using desorption isotherms by the BJH method.

## 4.5 $^{27}$al MAS NMR

Information on the relative occupancy of tetrahedral and octahedral aluminum sites in alumina was obtained using $^{27}$Al solid-state MAS NMR. The chemical shift ranges for aluminum in different coordination with oxygen (or hydroxyls) are typically 10 to 20 ppm for octahedral coordinated aluminum ($Al^{VI}$), 30–40 ppm for pentahedral coordinated aluminum ($Al^{V}$) and 50–80 ppm for tetrahedral coordinated aluminum ($Al^{IV}$) (Mogica-Betancourt et al. 2014). The $^{27}$Al MAS NMR spectra are shown in Figure 4(a-b). The most intense signal in the spectra at 0.0–2.0 ppm is attributed to the aluminum atoms in an octahedral coordination ($Al^{VI}$), a very small

signal at 28.0–35.0 ppm occurs, which is assigned to the 5-fold ($Al^{V}$) oxygen-coordinated aluminum atoms for $Al_2O_3$-A sample. For $Al_2O_3$-B sample no resonance for $Al^{V}$ was found and a signal at 57.0–62.0 ppm is assigned to the tetrahedral coordinated aluminum atoms ($Al^{IV}$) respectively. However, according to the literature the presence of the five-coordinated aluminum arises from the structure defects of γ-$Al_2O_3$ or highly distorted tetrahedral (Paglia et al. 2005). These structural defects are corroborated by the unusual broadening of some X-ray diffraction peaks, Figure 1, attributed to the presence of Mg as impurity in $Al_2O_3$-A sample. It is worthy to mention that the $Al^{V}$ cannot be clearly observed in alumina sample, due to a relatively small structural damage, observing a percentage of about 4.67 % of five-coordinated aluminum atoms, as show Table 5.

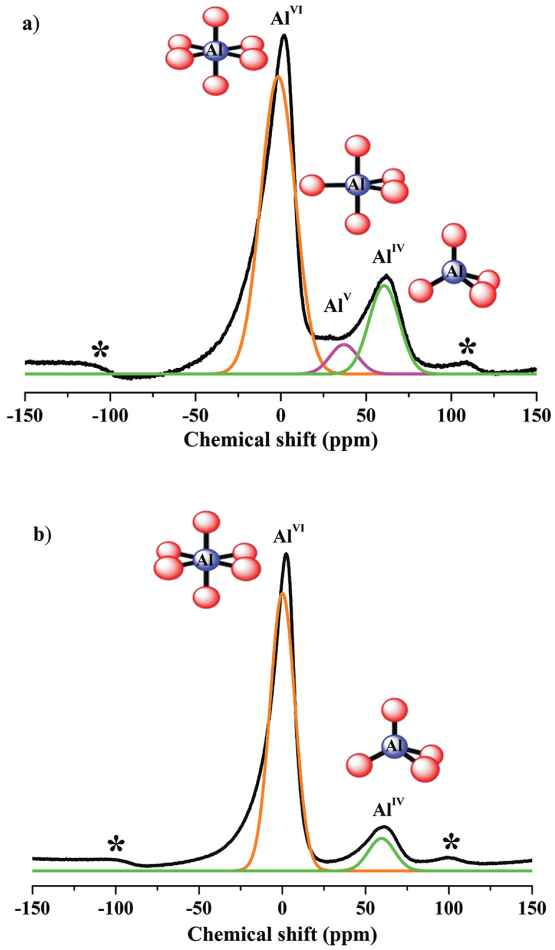


**Figure 4:** $^{27}$Al NMR spectra of a) $Al_2O_3$-A and b) $Al_2O_3$-B. The peaks marked with an asterisk are spinning side-bands.

**Table 5:** $^{27}$Al MAS NMR parameters characteristics of the alumina samples.

| Sample | $Al^{VI}$ | | $Al^{V}$ | | $Al^{IV}$ | |
|---|---|---|---|---|---|---|
| | δiso (ppm) | % | δiso (ppm) | % | δiso (ppm) | % |
| $Al_2O_3$-A | 2.00 | 75.29 | 28.16 | 4.67 | 60.79 | 20.04 |
| $Al_2O_3$-B | 2.42 | 74.70 | - | 0.0 | 61.12 | 25.30 |

*(-): Not Detected.

All the spectra have been simulated by Gaussian line shape with appropriate parameters to extract an accurate isotropic chemical shift and the relative intensity of various components. The amount of aluminum atoms with different coordination numbers were quantitatively calculated with fitting peak areas and the results are summarized in Table 4. The integration reveals values between 20 and 30 % for the tetrahedral sites which is in accordance with γ-$Al_2O_3$ model (Liu et al. 2008). Therefore, the magnesium presence in the $Al_2O_3$-A sample, gender the appearance of the relative population of $Al^{V}$, decreases the relative population of $Al^{IV}$.

## 4.6 FT-IR pyridine adsorption

The acidity of oxide is originated from the surface OH and the metal cations formed after dehydration of OH. Therefore, the variation of the surface OH concentration after thermal treatment can directly influence the surface acidity of γ-$Al_2O_3$. Given the importance of acidity in many catalytic reactions, the spectra of the pyridine adsorption–desorption were obtained for the samples at different temperatures, Figure 5, were recorded to obtain information of the Brønsted acid sites (BAS) and Lewis acid sites (LAS).

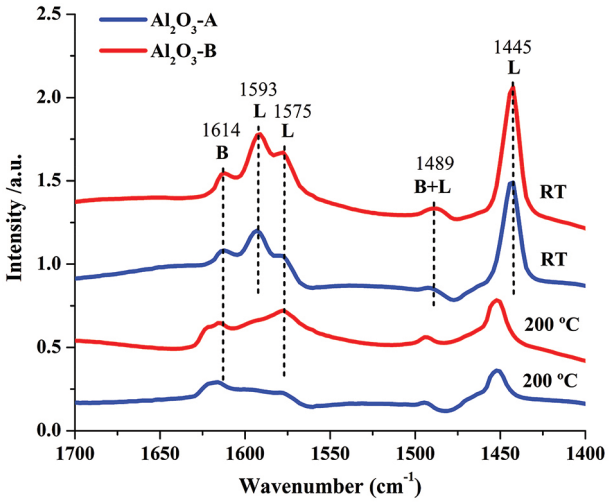


**Figure 5:** FT-IR spectra of the pyridine adsorption at different temperatures of $Al_2O_3$-A and $Al_2O_3$-B.

Both samples show the bands at 1445, 1575 and 1593 $cm^{-1}$ which are attributed to pyridine adsorbed on Lewis acid sites. The band at 1614 $cm^{-1}$ which are attributed to pyridine adsorbed on Brønsted acid sites and the band at 1489 $cm^{-1}$ is attributed to pyridine associated with both Lewis and Brønsted acid sites (Garbarino et al. 2017; Sararuk et al. 2017). It is widely accepted that the Lewis acid sites of alumina are generated by partly uncoordinated $Al^{3+}$ and cation vacancies exposed on the surface with water (always present in the environment) adsorbed to produce surface hydroxyl groups (Liu and Truitt 1997). Although the positions of different adsorption peaks do not change obviously, the total peak area of the two samples and the relative peak area of the adsorption peaks are different. This means that both the total acid amount and acidity distribution of the alumina changed depending on the precursor.

The weak Lewis acidity mainly arises from five-coordinated aluminum atoms while the medium strong Lewis acidity mainly relates to four-coordinated aluminum atoms. According to the result from $^{27}$Al MAS NMR, Figure 4(a), the appearance of the relative population of $Al^{V}$ decreases the relative population of $Al^{IV}$, this is attributed to the presence of Mg as impurity, as was determined, Table 2, due recent studies that have shown that the addition of Mg to alumina in order to increase the alumina's basicity as well as to decrease its acidity, as expected from the lower electronegativity of Mg (1.31) than of Al (1.51) atoms (Chen et al. 2016). Others authors report with regard to the basic sites, that Mg additionally increases the concentration of basic $OH^-$ and $O^{2-}$ Sites (Sanderson 1988). In order to check these changes, the acid properties of alumina with presence of Mg as impurity were investigated using IR spectroscopy of adsorbed pyridine; the results are summarized in Table 6.

**Table 6:** Amounts of Brønsted and Lewis acid sites of the alumina determined by pyridine- FTIR.

| Sample | Amount of acid sites (μmol g − 1) | | | | | |
|---|---|---|---|---|---|---|
| | 298 K | | | 473 K | | |
| L | B | L + B | L | B | L + B | |
| $Al_2O_3$-A | 333 | 0.03 | 333.03 | 39 | 0.0 | 39 |
| $Al_2O_3$-B | 398 | 0.05 | 398.05 | 59 | 0.0 | 46 |

[1] Source: Author's own elaboration

The relative population of $Al^V$ increases from zero to 4.67 %, while the medium strong acid site decreases to 20.04 % for $Al_2O_3$-A sample, as is shown in Table 5. Consequently, the weak acid site increases, while the medium strong acid site decreases. Since the surface acidity of the obtained alumina is mainly dominated by the weak acidity (Digne et al. 2004). The presence of Brønsted sites is obviously related to the existence of residual sulfate species on the surface. Possibly, terminal OH groups could be involved in the coordination of $HSO_4^-$ (Guzman-Castillo et al. 2005) formed in solution, as was determined by XRF and EDX in the both samples. These features influence directly the surface acidity distribution of alumina. It can be observed that with the evacuation at 200 °C the intensity of bands decreases slightly. However, others authors have reported that with evacuation at higher temperature (>300 °C) the intensity of these bands decreases completely (Cervantes-Gaxiola et al. 2013).

## 4.7 XPS analysis: survey spectra

XPS surface analysis is used to evaluate elemental composition and identify chemical states in a wide variety of materials. In the case of elemental composition, the calculation could be straight as in this work, when peaks do not overlap with others in the vicinity of the regions. Regarding to chemical compound identification, particularly for aluminum, is well known that precise identification of its oxides ($\alpha$-$Al_2O_3$ and $\gamma$-$Al_2O_3$), hydroxide (three forms of $Al(OH)_3$-Nordstrandite, Bayerite, and Gibbsite) and oxy-hydroxides ($\beta$-AlOOH-Diaspore and $\gamma$-AlOOH-Boehmite) is not possible for the core levels Al 2p, Al 2s and O 1s (Sherwood 1998) due the small differences in binding energy. However, Duong and Kloprogge have shown that is possible to distinguish the oxygen in the crystal structure, hydroxyl groups and adsorbed water (Duong, Wood, and Kloprogge 2005) as we do in this work.

As start point were acquired the survey spectra for elemental composition calculations, for which the analyzer pass energy was of 117.4 eV. Then high resolution spectra of C 1s, O 1s, Al 2p, N 1s and S 2p were recorded with 23.5 eV of pass energy. For $Al_2O_3$-A and $Al_2O_3$-B samples the survey and high resolution spectra were acquired at three different points through the sample and the average spectra and quantification on these points are presented in this work. Charge correction was done using the adventitious carbon positioned at 284.8 eV.

Figure 6 shows the two XPS survey spectrum of $Al_2O_3$-A and $Al_2O_3$-B. Where it is confirmed the presence of Al, O, C, N & S at binding energies of ~74.1 eV, 530.7 eV, 284.8 eV, 399.0 eV, and 170.1 eV, respectively. For both samples, the major contribution comes from Al, O, C and minor contribution of N and S which presence is attributed to residues generated during the process of synthesis.

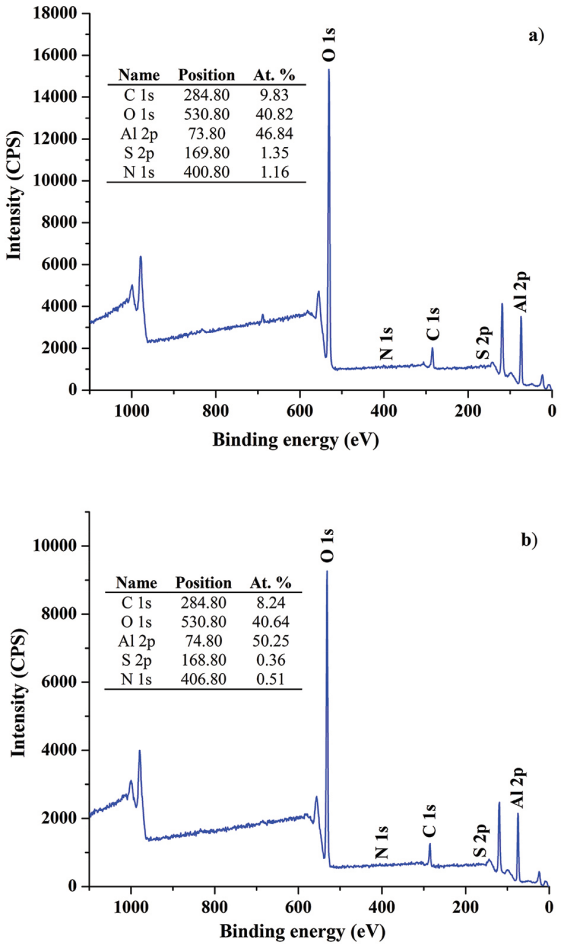


**Figure 6:** XPS survey spectra of the a) $Al_2O_3$-A and b) $Al_2O_3$-B.

Assessment of atomic percentages from survey was achieved using CasaXPS software, which uses relative sensitivity factors and a model that assumes a homogeneous layer:$R_A{}^{a\%} = N_A / \sum_j N_B \bullet 100$; where$N_A = I_A / S_A$. The background for each region quantified (i. e. C 1s, O 1s, N 1s, Al 2p and S 2p) was subtracted using a Shirley background type. Each region in survey spectra was limited manually at end points to consider only the photoemission area of each core level. The average atomic weight percentages are presented in the survey spectrum, Figure 6.

### 4.7.1 High resolution spectra of al 2p and o 1s core levels

High resolution analysis of core levels O 1s and Al 2p have been accomplished using AAnalyzer® software. For all spectra the line shape used was the Voigt profile. Values for Gauss and Lorentzian are different in some cases for each component in the spectra and are displayed in Table 6. Each pair of the same core levels in samples A and B for all the elements of interest were handled using the simultaneous-fitting mod which allows obtaining a unique set of peak parameters that minimizes the fitting error for all the data (Muñoz-Flores and Herrera-Gomez 2012).

The aluminum high resolution spectra show two overlapping bands associated with two different Al 2p transitions with binding energies of 74.1 and 75.7 eV in both samples, Figure 7a,c. The ratio of the two types of aluminum is in the order of 42.67 and 57.30 % for $Al_2O_3$-A, and for $Al_2O_3$-B, 30.20 and 69.80 %. The 74.1 eV transition is attributed to the aluminum atoms in tetrahedral coordination ($Al^{VI}$) and the 75.7 eV transition is assigned to the octahedral coordinated aluminum atoms ($Al^{IV}$).

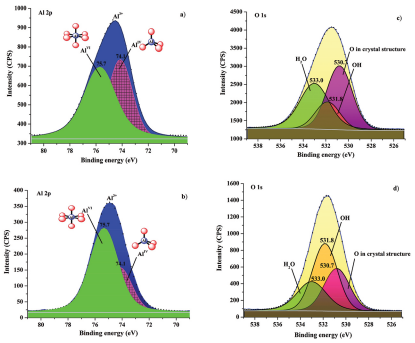

**Figure 7:** High resolution spectra of Al 2p in: a) $Al_2O_3$-A and b) $Al_2O_3$-B; High resolution spectra O 1s in: c) $Al_2O_3$-A and d) $Al_2O_3$-B.

The binding energy difference between Al 2p and O1s is 457 eV for $Al_2O_3$-A and 456 for $Al_2O_3$-B, which is in agreement with literature (Barr 1997). The oxygen high resolution scans are rather complex and contain a number of overlapping transitions. Band component analysis indicates the presence of three transitions at 530.7, 531.8 and 533.0 eV associated with O in crystal structure, hydroxyl groups and as chemisorbed water, respectively. The relative quantity of each one in the sample represents roughly 43.62, 17.89 and 38.47 % of the total amount of oxygen present in the crystal structure in the $Al_2O_3$-A and 29.80, 45.00 and 25.20 % for $Al_2O_3$-B, as is shown in Table 7. Following an analogue interpretation of the oxygen transitions in both samples, the three transitions are interpreted as being due to the central O around the $Al^{IV}$, hydroxyl group around the $Al^{VI}$, water in both around the $Al^{VI}$ and as crystal water. The O/Al atomic ratios were calculated to be 1.13 and 1.20 for $Al_2O_3$-A, and $Al_2O_3$-B, respectively. Obtained values are close to the stoichiometric value of 1.5 (Barr 1997; Duong, Wood, and Kloprogge 2005; Kerber et al. 1996; Kloprogge et al. 2006; 2012; 1998).

**Table 7:** Results of high resolution analysis of core levels Al 2p and O 1s for each component in the spectra of $Al_2O_3$-A and $Al_2O_3$-B samples.

| | | | % Concentration | |
|---|---|---|---|---|
| **Species** | **BE (eV)** | **FWHM (eV)** | **$Al_2O_3$-A** | **$Al_2O_3$-B** |
| Al in $Al^{3+}$ ($Al^{VI}$) | 74.1 | 2.0 | 42.68 | 30.20 |
| Al in OH ($Al^{IV}$) | 75.7 | 2.5 | 57.32 | 69.80 |
| O in crystal structure | 530.8 | 2.5 | 43.62 | 29.80 |
| O in OH | 531.8 | 2.5 | 17.89 | 45.00 |
| O in adsorbed water | 533.0 | 2.7 | 38.47 | 25.20 |

*BE: Binding energy (eV).
*FWHM: full width at half maximum (eV).

Table 7 shows a higher concentration of $Al^{3+}$ species of about 42.68 % for $Al_2O_3$-A, and 30.20 % for $Al_2O_3$-B; this is attributed to higher crystallinity in the $Al_2O_3$-A sample, as is observed in the diffraction pattern, Figure 1(a). The concentration of O in the crystal structure is higher in $Al_2O_3$-A sample, associated with the greater number of O bonds with $Al^{3+}$ species in the crystalline structure than $Al_2O_3$-B. It can be observed in Table 6, a higher content of Al-OH species in $Al_2O_3$-B, indicating a higher percentage of aluminum atoms in tetrahedral coordination ($Al^{IV}$), these results agree with the $^{27}Al$ NMR spectrum, Figure 4, generating acidity more strong than $Al_2O_3$-A sample.

The previous studies indicated that a higher Al atom content into the framework ($Al^{IV}$ coordinated) creates Brønsted acid sites (Knözinger and Ratnasamy 1978). According to this, it can be attributed that the slight difference of Brønsted acid sites (band at 1614 $cm^{-1}$), Figure 5, between both materials is attributed to a higher percentage of groups Al-OH in $Al_2O_3$-B of 69.80 and 57.32 at. % in $Al_2O_3$-A, obtained by XPS analysis, as shown Table 6. The non-presence of Mg by this technique (XPS), can be explained by the assumption is that the trace element is homogenously distributed in the matrix, and the limit is expressed as an atomic fraction.

## 5 Activity tests: dibenzothiophene HDS

Both alumina samples were used as catalyst support of Ni and Mo. In this sense, solids of NiMo/$Al_2O_3$-A and NiMo/$Al_2O_3$-B were prepared according to the procedure previously described.

The HDS of DBT was studied under conditions at 350 ºC and 3.1 MPa, which are closed to those used for industrial processes. DBT was chosen because it is considered an appropriate compound for the investigation of activity and reaction mechanisms of the proposed HDS catalysts, and also due to its difficulty for HDS. In addition, DBT is the most common of the sulfur-containing compounds present in petroleum feedstocks.

Table 8 summarizes the activity and selectivity results for the catalysts under steady-state conditions after 5 h of reaction. The main reaction products from HDS of DBT were biphenyl (BP) and cyclohexylbenzene (CHB), while small amounts of tetrahydro-dibenzothiophene (THDBT) were produced during the reaction. The dibenzothiophene HDS model reaction has been used to establish the performance of sulfide Ni–Mo catalysts. For DBT desulfurization, it has been proposed that the reaction proceeds in accordance with the hydrogenolysis pathway, through the direct desulfurization route (DDS), leading to the production of biphenyl, or by a second hydrogenation reaction pathway (HYD), in which one of the aromatic rings of dibenzothiophene is firstly prehydrogenated, forming tetrahydro- and hexahydro-dibenzothiophene, which is later desulfurized to form cyclohexylbenzene (CHB). The evolution of the conversion of DBT over the supported catalysts based in the alumina materials is shown in Figure 8.

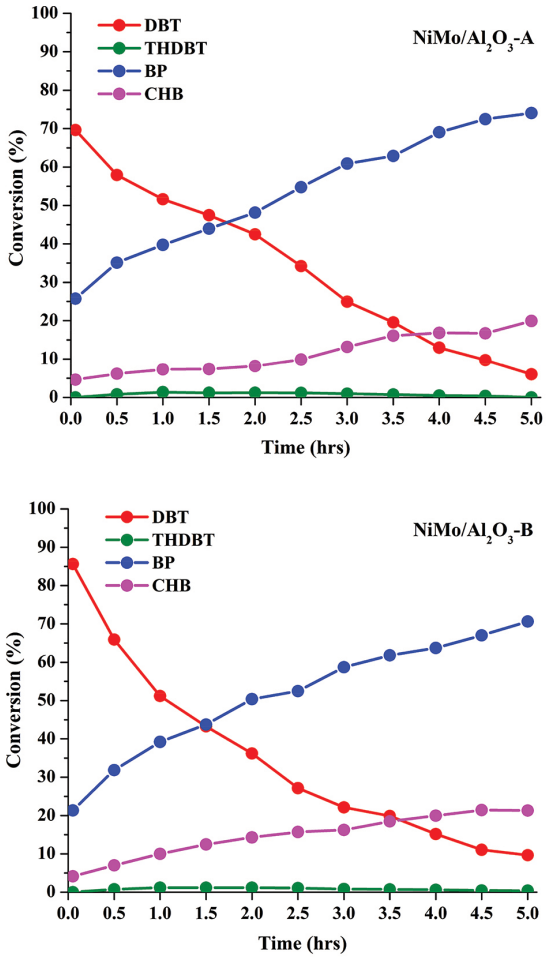


**Figure 8:** Conversion of DBT during HDS for NiMo/$Al_2O_3$-A and NiMo/$Al_2O_3$-B and products distribution on: Dibenzothiophene (DBT), tetrahydrodibenzothiophene (THDBT), biphenyl (BP) and Cyclohexylbenzene (CHB). *Reaction conditions:* T = 350 °C; P = 3.1 MPa, Time reaction = 5 $h^{-1}$. The reaction starts at 350 °C = (time 0.0).

**Table 8:** Reaction-rate constant, % DBT conversion and selectivity for the catalysts during HDS–DBT.

| Catalyst | $k$ (x$10^{-6}$ molg$^{-1}$s$^{-1}$) | % DBT conversion | HYD/DDS |
|---|---|---|---|
| NiMo/$Al_2O_3$-A | 3.77 | 95 | 0.26 |

| | | | |
|---|---|---|---|
| $NiMo/Al_2O_3$-B | 4.05 | 90 | 0.30 |

[1] Source: Author's own elaboration

It is observed that the catalyst $NiMo/Al_2O_3$-B exhibited a lower DBT conversion (90 %) than $NiMo/Al_2O_3$-A. On the other hand, the catalyst A shows an improvement of activity with a DBT conversion of 95 %. Such effect can be attributed to the presence of Mg species as impurity, due to that played a structural promoting role in the support and altered the nature of active phase interaction with the support surface and slightly increasing the Dibenzothiophene HDS activity as is well reported in the literatures (Kumar et al. 2004; Shi et al. 2014). The catalytic activity results indicated that the HDS of DBT it's related to the dispersion of Mo by the presence of Mg, decreasing the acidity and increase the basicity as shown by FT-IR pyridine adsorption and $^{27}Al$ MAS NMR analysis, whereas the slightly hydrogenation of DBT it's related to the acidity of catalyst $NiMo/Al_2O_3$-B.

Regarding selectivity, the two catalysts favored the DDS pathway; however, it was possible to observe some differences. For instance, the catalyst $NiMo/Al_2O_3$-B exhibits a slightly higher HYD selectivity (0.30) than the catalyst $NiMo/Al_2O_3$-A (0.26) (Table 8).

## 6 Conclusion

In this research, two γ-alumina samples were synthesized from two precursors with different percentage of purity. One of them, it is a salt of low cost commercially available which contains magnesium as the main impurity. Both materials showed similar structural characteristics such as crystalline phase and nanoparticle morphology; however, the presence of magnesium provoked a decrease in the relative population of $Al^{IV}$, decreasing the acidity and increases the basicity. In addition, the magnesium considered as an impurity in the alumina support produced an apparently better performance in the supported catalysts of NiMo during the DBT hydrodesulfurization, attributed to the fact that the Mg altered the nature of active phase interaction with the support surface, promoting a greater dispersion of Mo species. Therefore, aluminum salts containing magnesium as impurity could be considered as raw precursors for preparing catalyst supports of lower cost.

### Acknowledgements

Authors gratefully acknowledge the support provided by the National Council on Science and Technology (CONACYT), LICAMM UG: Laboratory of research and characterization of minerals and material, for providing access to XRF and XRD and University of Guanajuato, México. We also thank LINAN for providing access to XPS facilities and CONACYT for the financial support to LINAN.

**Conflicts of Interest:** The authors declare that they have no conflict of interest.

## References

Aberuagba, F., M. Kumar, J. K. Gupta, G. Muralidhar, and L. D. Sharma. 2002. "Preparation and Characterization of $MgO/Al_2O_3$ Mixed Oxides Support for Hydrotreating Catalysts." Reaction Kinetics and Catalysis Letters 75 (2): 245–250.

Barr, T. 1997. "ESCA Studies of the Coordination State of Aluminium in Oxide Environments. Journal of the Chemical Society." Faraday Transactions 93 (1): 181–186.

Boumaza, A., L. Favaro, J. Lédion, G. Sattonnay, J. B. Brubach, P. Berthet, and R. Tétot. 2009. "Transition Alumina Phases Induced by Heat Treatment of Boehmite: An X-Ray Diffraction and Infrared Spectroscopy Study." Journal of Solid State Chemistry 182 (5): 1171–1176.

Breysse, M., P. Afanasiev, C. Geantet, and M. Vrinat. 2003. "Overview of Support Effects in Hydrotreating Catalysts." Catalysis Today 86 (1): 5–16.

Čejka, J. 2003. "Organized Mesoporous Alumina: Synthesis, Structure and Potential in Catalysis." Applied Catalysis A: General 254 (2): 327–338.

Cervantes-Gaxiola, M. E., M. Arroyo-Albiter, A. Pérez-Larios, P. B. Balbuena, and J. Espino-Valencia. 2013. "Experimental and Theoretical Study of NiMoW, NiMo, and NiW Sulfide Catalysts Supported on an Al-Ti-Mg Mixed Oxide during the Hydrodesulfurization of Dibenzothiophene." Fuel 113: 733–743.

Chen, W., H. Nie, D. Li, X. Long, J. Van Gestel, and F. Maugé. 2016. "Effect of Mg Addition on the Structure and Performance of Sulfide $Mo/Al_2O_3$ in HDS and HDN Reaction." Journal of Catalysis 344: 420–433.

Del Angel, G., C. Guzmán, A. Bonilla, G. Torres, and J. M. Padilla. 2005. "Lanthanum Effect on the Textural and Structural Properties of γ-$Al_2O_3$ Obtained from Boehmite." Materials Letters 59 (4): 499–502.

Digne, M., P. Sautet, P. Raybaud, P. Euzen, and H. Toulhoat. 2004. "Use of DFT to Achieve a Rational Understanding of Acid–Basic Properties of γ-alumina Surfaces." Journal of Catalysis 226 (1): 54–68.

Dubey, S. P., A. D. Dwivedi, M. Sillanpää, H. Lee, Y. N. Kwon, and C. Lee. 2017. "Adsorption of as (V) by Boehmite and Alumina of Different Morphologies Prepared under Hydrothermal Conditions." Chemosphere 169: 99–106.

Duong, L. V., B. J. Wood, and J. T. Kloprogge. 2005. "XPS Study of Basic Aluminum Sulphate and Basic Aluminium Nitrate." Materials Letters 59 (14): 1932–1936.

Farag, H. K., M. Al Zoubi, and F. Endres. 2009. "Sol-Gel Synthesis of Alumina, Titania and Mixed Alumina/Titania in the Ionic Liquid 1-Butyl-1-Methylpyrrolidinium Bis (Trifluoromethylsulphonyl) Amide." Journal of Materials Science 44 (1): 122–128.

Gao, Ming, Akihiko Ito, and Takashi Goto. 2015. "Preparation of γ-$Al_2O_3$ Films by Laser Chemical Vapor Deposition." Applied Surface Science 340: 160–165.

Garbarino, G., C. Wang, I. Valsamakis, S. Chitsazan, P. Riani, E. Finocchio, and G. Busca. 2017. "Acid-Basicity of Lanthana/Alumina Catalysts and Their Activity in Ethanol Conversion." Applied Catalysis B: Environmental 200: 458–468.

Guzman-Castillo, M. L., F. Hernández-Beltrán, J. J. Fripiat, A. Rodriquez-Hernández, R. G. De León, J. Navarrete-Bolanos, and X. Bokhimi. 2005. "Physicochemical Properties of Aluminas Obtained from Different Aluminum Salts." Catalysis Today 107: 874–878.

Hosseini, S. Y. G., and M. R. Khosravi Nikou. 2012. "Synthesis and Characterization of Different γ-$Al_2O_3$ Nanocatalysts for Methanol Dehydration to Dimethyl Ether." International Journal of Chemical Reactor Engineering 10 (1): 1542–6580 DOI: https://doi.org/10.1515/1542-6580.3072.

Jun-Cheng, L., X. Lan, X. Feng, W. Zhan-Wen, and W. Fei. 2006. "Effect of Hydrothermal Treatment on the Acidity Distribution of γ-$Al_2O_3$ Support." Applied Surface Science 253 (2): 766–770.

Kerber, S. J., J. J. Bruckner, K. Wozniak, S. Seal, S. Hardcastle, and T. L. Barr. 1996. "The Nature of Hydrogen in X-Ray Photoelectron Spectroscopy: General Patterns from Hydroxides to Hydrogen Bonding." Journal of Vacuum Science & Technology A: Vacuum, Surfaces, and Films 14 (3): 1314–1320.

Kloprogge, J. T., L. V. Duong, B. J. Wood, and R. L. Frost. 2006. "XPS Study of the Major Minerals in Bauxite: Gibbsite, Bayerite and (Pseudo-) Boehmite." Journal of Colloid and Interface Science 296 (2): 572–576.

Knözinger, H., and P. Ratnasamy. 1978. "Catalytic Aluminas: Surface Models and Characterization of Surface Sites." Catalysis Reviews Science and Engineering 17 (1): 31–70.

Kumar, M., F. Aberuagba, J. K. Gupta, K. S. Rawat, L. D. Sharma, and G. M. Dhar. 2004. "Temperature-Programmed Reduction and Acidic Properties of Molybdenum Supported on MgO–$Al_2O_3$ and Their Correlation with Catalytic Activity." Journal of Molecular Catalysis A: Chemical 213 (2): 217–223.

Lesaint, C., W. R. Glomm, Ø. Borg, S. Eri, E. Rytter, and G. Øye. 2008. "Synthesis and Characterization of Mesoporous Alumina with Large Pore Size and Their Performance in Fischer–Tropsch Synthesis." Applied Catalysis A: General 351 (1): 131–135.

Liu, M., and H. Yang. 2010. "Facile Synthesis and Characterization of Macro–Mesoporous γ-$Al_2O_3$." Colloids and Surfaces A: Physicochemical and Engineering Aspects 371 (1): 126–130.

Liu, Q., A. Wang, X. Wang, P. Gao, X. Wang, and T. Zhang. 2008. "Synthesis, Characterization and Catalytic Applications of Mesoporous γ-alumina from Boehmite Sol." Microporous and Mesoporous Materials 111 (1): 323–333.

Liu, X., and R. E. Truitt. 1997. "DRFT-IR Studies of the Surface of γ-Alumina." Journal of the American Chemical Society 119 (41): 9856–9860.

Mogica-Betancourt, J. C., A. López-Benítez, J. R. Montiel-López, L. Massin, M. Aouine, M. Vrinat, and A. Guevara-Lara. 2014. "Interaction Effects of Nickel Polyoxotungstate with the $Al_2O_3$–MgO Support for Application in Dibenzothiophene Hydrodesulfurization." Journal of Catalysis 313: 9–23.

Muñoz-Flores, J., and A. Herrera-Gomez. 2012. "Resolving Overlapping Peaks in ARXPS Data: The Effect of Noise and Fitting Method." Journal of Electron Spectroscopy and Related Phenomena 184 (11): 533–541.

Paglia, G., A. L. Rohl, C. E. Buckley, and J. D. Gale. 2005. "Determination of the Structure of γ-alumina from Interatomic Potential and First-Principles Calculations: The Requirement of Significant Numbers of Non-Spinel Positions to Achieve an Accurate Structural Model." Physical Review B 71 (22): 224115.

Pan, D., Z. Dong, M. He, W. Chen, S. Chen, F. Yu, and R. Li. 2017. "Structural and Surface Properties of Highly Ordered Mesoporous Magnesium-Aluminium Composite Oxides Derived from Facile Synthesis." Materials Chemistry and Physics 186: 574–583.

Pan, D., Q. Xu, Z. Dong, S. Chen, F. Yu, X. Yan, and R. Li. 2015. "Facile Synthesis of Highly Ordered Mesoporous Cobalt–Alumina Catalysts and Their Application in Liquid Phase Selective Oxidation of Styrene." RSC Advances 5 (119): 98377–98390.

Panias, D., and A. Krestou. 2007. "Effect of Synthesis Parameters on Precipitation of Nanocrystalline Boehmite from Aluminate Solutions." Powder Technology 175 (3): 163–173.

Pecharroman, C., I. Sobrados, J. E. Iglesias, T. Gonzalez-Carreno, and J. Sanz. 1999. "Thermal Evolution of Transitional Aluminas Followed by NMR and IR Spectroscopies." The Journal of Physical Chemistry B 103 (30): 6160–6170.

Perander, L. M., Z. D. Zujovic, M. M. Hyland, M. E. Smith, L. A. O'Dell, and J. B. Metson. 2008. "Short-And Long-Range Order in Smelter Grade Alumina: Development of Nano and Microstructures during the Calcination of Bayer Gibbsite." TMS Light Metals 29–35. https://www.researchgate.net/publication/283857290_Short-_and_long-range_order_in_smelter_grade_alumina_-_Development_of_nano-_and_microstructures_during_the_calcination_of_bayer_gibbsite.

Rana, M. S., M. L. Huidobro, J. Ancheyta, and M. T. Gómez. 2005. "Effect of Support Composition on Hydrogenolysis of Thiophene and Maya Crude." Catalysis Today 107: 346–354.

Renuka, N. K., A. V. Shijina, and A. K. Praveen. 2012. "Mesoporous γ-alumina Nanoparticles: Synthesis, Characterization and Dye Removal Efficiency." Materials Letters 82: 42–44.

Sakashita, Y., Y. Araki, and H. Shimada. 2001. "Effects of Surface Orientation of Alumina Supports on the Catalytic Functionality of Molybdenum Sulfide Catalysts." Applied Catalysis A: General 215 (1): 101–110.

Sanderson, R. T. 1988. "Principles of Electronegativity Part I. General Nature." Journal of Chemical Education 65 (2): 112.

Sararuk, C., D. Yang, G. Zhang, C. Li, and S. Zhang. 2017. "One-Step Aldol Condensation of Ethyl Acetate with Formaldehyde over Ce and P Modified Cesium Supported Alumina Catalyst." Journal of Industrial and Engineering Chemistry 46: 342–349.
Sherwood, P. M. 1998. "Introduction to Studies of Aluminum and Its Compounds by XPS." Surface Science Spectra 5 (1): 1–3.
Shi, J., Y. Zhou, Y. Zhang, S. Zhou, Z. Zhang, J. Kong, and M. Guo. 2014. "Synthesis of Magnesium-Modified Mesoporous $Al_2O_3$ with Enhanced Catalytic Performance for Propane Dehydrogenation." Journal of Materials Science 49 (16): 5772–5781.
Sifontes, Á. B., B. Gutiérrez, A. Mónaco, A. Yanez, Y. Díaz, F. J. Méndez, and J. L. Brito. 2014. "Preparation of Functionalized Porous nano-γ-$Al_2O_3$ Powders Employing Colophony Extract." Biotechnology Reports 4: 21–29.
Sing, K.S.W., D.H. Everett, R.A.W. Haul, L. Moscou, R. A Pierotti, J. Rouquerol, and T. Siemieniewska. 1985. "Reporting Physisorption Data for Gas/Solid Systems with Special Reference to the Determination of Surface Area and Porosity (Recommendations 1984)." Pure and Applied Chemistry 57 (4): 603–619.
Sun, M., T. Zhao, Z. Li, Z. Ma, J. Wang, and F. Li. 2016. "Sol-Gel Synthesis of Macro-Mesoporous $Al_2O_3$-$SiO_2$-$TiO_2$ Monoliths via Phase Separation Route." Ceramics International 42 (14): 15926–15932.
Trejo, F., M. S. Rana, and J. Ancheyta. 2008. "CoMo/MgO–$Al_2O_3$ Supported Catalysts: An Alternative Approach to Prepare HDS Catalysts." Catalysis Today 130 (2): 327–336.
Wang, L., Z. Tan, S. Meng, D. Liang, and G. Li. 2001. "Enhancement of Molar Heat Capacity of Nanostructured $Al_2O_3$." Journal of Nanoparticle Research 3 (5): 483–487.
Wang, X., D. Pan, Q. Xu, M. He, S. Chen, F. Yu, and R. Li. 2014. "Synthesis of Ordered Mesoporous Alumina with High Thermal Stability Using Aluminum Nitrate as Precursor." Materials Letters 135: 35–38.
Witharana, S., C. Hodges, D. Xu, X. Lai, and Y. Ding. 2012. "Aggregation and Settling in Aqueous Polydisperse Alumina Nanoparticle Suspensions." Journal of Nanoparticle Research 14 (5): 851.
Wolverton, C., and K. C. Hass. 2000. "Phase Stability and Structure of Spinel-Based Transition Aluminas." Physical Review B 63 (2): 024102.
Xu, B., Y. Yang, Y. Xu, B. Han, Y. Wang, X. Liu, and Z. Yan. 2017. "Synthesis and Characterization of Mesoporous Si-Modified Alumina with High Thermal Stability." Microporous and Mesoporous Materials 238: 84–89.
Xu, X., Q. Yu, Z. Lv, J. Song, and M. He. 2016. "Synthesis of High-Surface-Area Rod-Like Alumina Materials with Enhanced Cr (VI) Removal Efficiency." Microporous and Mesoporous Materials DOI: 10.1016/j.micromeso.2016.12.002.
Zhang, L., Y. Wu, L. Zhang, Y. Wang, and M. Li. 2016. "Synthesis and Characterization of Mesoporous Alumina with High Specific Area via Coprecipitation Method." Vacuum 133: 1–6.
Zhang, X., F. Zhang, and K. Y. Chan. 2004. "The Synthesis of Large Mesopores Alumina by Microemulsion Templating, Their Characterization and Properties as Catalyst Support." Materials Letters 58 (22): 2872–2877.
Zhang, Y., F. Gao, H. Wan, C. Wu, Y. Kong, X. Wu, and Y. Chen. 2008. "Synthesis, Characterization of Bimetallic Ce–Fe-SBA-15 and Its Catalytic Performance in the Phenol Hydroxylation." Microporous and Mesoporous Materials 113 (1): 393–401.

## Bionotes

Universidad de Guadalajara, Centro Universitario de los Altos, Carretera a Yahualica, KM. 7.5, Tepatitlán de Morelos, Jalisco, C.P. 47600, México